Thin Solid Films 698 (2020) 137848

Contents lists available at ScienceDirect

Thin Solid Films

journal homepage: www.elsevier.com/locate/tsf

Atomic scale growth of $GdFeO_3$ perovskite thin films

Christoph Bohr[a,1], Pengmei Yu[b,1], Mateusz Scigaj[b], Corinna Hegemann[a], Thomas Fischer[a], Mariona Coll[b,*], Sanjay Mathur[a,*]

[a] Institute of Inorganic Chemistry, University of Cologne, Greinstraße 6, D-50939 Cologne, Germany
[b] Institut de Ciencia de Materials de Barcelona, ICMAB-CSIC, Campus UAB, 08193 Barcelona, Spain

ARTICLE INFO

Keywords:
Gadolinium orthoferrite
Single source precursor
Atomic layer deposition
Thin films
Nanomaterials
Alkoxides

ABSTRACT

Thin films of multiferroic gadolinium orthoferrite ($GdFeO_3$) are of significant interest due to intrinsic coupling of magnetic and ferroelectric order in their monolithic bimetallic structures relevant for potential applications in magneto-optical data storage devices. Formation of this composition in stoichiometric pure form is challenging due to facile formation of the thermodynamically preferred garnet phase ($Gd_3Fe_5O_{12}$) that mostly coexists as a minor phase in gadolinium orthoferrite films. We report herein the selective epitaxial growth of $GdFeO_3$ films by atomic layer deposition of a single bimetallic precursor $[GdFe(O^tBu)_6(C_5H_5N)_2]$ containing Gd:Fe in the required stoichiometric ratio, and using ozone as co-reactant. Intact vaporisation of $[GdFe(O^tBu)_6(C_5H_5N)_2]$ in the gas phase and its clean conversion into the complex oxide phase as validated by mass spectral studies and thermogravimetry demonstrate the potential of the Gd-Fe compound as an efficient single-source precursor. Epitaxial growth of $GdFeO_3$ on $SrTiO_3$ substrates was confirmed by X-ray diffraction analysis, whereas the presence of Fe^{3+} and Gd^{3+} without any traces of N species from the ligands was verified by X- ray photoelectron spectroscopy. Magnetic properties of the resulting perovskite films studied by superconducting quantum interference device measurements revealed the superposition of two independent magnetic contributions due to paramagnetic (Gd^{3+}) and ferromagnetic (Fe^{3+}) sublattices in $GdFeO_3$.

1. Introduction

Orthoferrites ($MFeO_3$; M = Ln, Sc, Y) have been extensively studied because of their wide variety of potential applications including magneto-optical devices [1], photocatalysis [2–4], gas sensing [5,6] and contrast agent in clinical magnetic resonance imaging [7]. It is known that the stability of the orthoferrite phase depends on the radius of *Ln* ions. For compositions where the lanthanides (Ln) are larger than terbium (Tb), the garnet structure becomes thermodynamically more stable, whereas smaller ionic lanthanide radius favors the formation of $LnFe_2O_4$ spinel phases [8]. In particular, the synthesis of multiferroic $GdFeO_3$ (GFO) [9], (Gd^{3+} = 0.94 Å, similar to Tb^{3+} = 0.92 Å), results in the coexistence of garnet ($Gd_3Fe_5O_{12}$) or magnetite (Fe_3O_4) secondary phases [10,11]. Thus, a phase-selective formation for GFO remains a synthetic challenge and requires new procedures.

Many of the applications mentioned above demand the growth of homogeneous thin films on planar and high aspect ratio surfaces. Atomic layer deposition (ALD) has become a fast-growing thin film engineering technique in the semiconductor industry and is rapidly expanding to newer and wider applications [12–15], owing to its unique capacity to nanoscale control of thickness and composition along with great effectiveness to homogeneously coat complex geometries and high aspect ratio structures. The stabilization of metastable phases by thin film epitaxial growth using ALD has already been demonstrated [16–23]. So far, ALD has been mostly used for binary compositions, where two complementary precursor chemistries are sequentially used in self-limiting surface reactions to build the binary lattice [24,25]. However, growing ternary or more complex compounds is far more challenging, due to the lack of compatible ALD precursors [22,23,26,27] and less known reaction pathways [28].

In view of the above, the development of new precursor systems and cautious evaluation of the metal-ligand chemistry appears to be of great value to control the film stoichiometry for complex compositions [24,29–31]. An attractive approach to simplify the surface reactions that would enable formation of ternary compounds is the use of single-source heterometallic precursors. Intrinsic advantages of bimetallic compounds include simplified precursor delivery system, lowered deposition temperatures, retained stoichiometry and pre-defined chemical

* Corresponding authors.
E-mail addresses: mcoll@icmab.es (M. Coll), sanjay.mathur@uni-koeln.de (S. Mathur).
[1] Equally contributed to this work.

https://doi.org/10.1016/j.tsf.2020.137848
Received 17 July 2019; Received in revised form 28 January 2020; Accepted 6 February 2020
Available online 08 February 2020
0040-6090/

compatibility between the target film and selected precursor [32]. The lack of adequate volatility and possible premature fragmentation can however limit the application of this concept in the ALD process [24,29,31]. Moreover, the lack of mechanistic models for the decomposition of bimetallic precursors in an ALD process makes the whole process even more challenging.

In this work, we report on a volatile single-source Gd-Fe bimetallic precursor $[GdFe(O^tBu)_6(C_5H_5N)_2]$ and their subsequent deposition to $GdFeO_3$ thin films by ALD. We demonstrate the stabilization of epitaxially grown $GdFeO_3$ thin films on $SrTiO_3$ substrates exhibiting atomically smooth surface morphology upon high temperature thermal treatment. The deposition of the ternary oxide from this heteronuclear precursor reinforces our strategy to develop stoichiometric complex materials with atomic control that can potentially lead to new and improved properties.

2. Experimental section

2.1. Precursor synthesis

2.1.1. General remarks

The synthesis of alkoxide and amide precursors was performed using modified Stock techniques. The hydrocarbon solvents were dried using standard procedures [33] and stored over sodium wire. $[Fe(O^tBu)_3]_2$ [34] and $[Gd\{N(SiMe_3)_2\}_3]$ [35] was synthesized by literature known procedures. Data collection for X-ray structure elucidation was performed on a *Stoe IPDS 2T* diffractometer using graphite monochromated Mo Kα radiation (0.71071 Å). The programs used in this work are STOE's X-Area [36] and the WINGX suite of programs [37], including SIR-92 [38], SHELX and SHELXTL [39] for structure solution and refinement. H atoms were calculated geometrically and a riding model was applied during the refinement process. The supplementary crystallographic data for this paper (CCDC: 1912740) can be obtained free of charge from The Cambridge Crystallographic Data Centre via www.ccdc.cam.ac.uk/data_request/cif. Elemental analysis was carried out on a HEKAtech *CHNS* Euro EA 3000 with helium as carrier gas. Deviations of the *CHNS* data from the calculated values can be attributed to the extraordinary sensitivity of the compound towards moisture and the weakly bound pyridine. Mass spectra were recorded on a *Finnigan* MAT 95 (Electron ionization, 20 eV).

2.1.2. Synthesis of $[GdFe(O^tBu)_6(C_5H_5N)_2]$

A solution of 1.05 g (1.64 mmol) $[Gd\{N(SiMe_3)_2\}_3]$, dissolved in 5 mL toluene and 1.5 mL pyridine was heated until the colorless solution turned red. Mixing with a solution of 0.45 g (0.82 mmol) $[Fe(O^tBu)_3]_2$ in 5 mL toluene and 1 mL pyridine lead to a black solution. The molar ratio of 2:1 was chosen due to the dimeric structure of the iron compound. After addition of 2.5 mL *tert*-butanol the reaction mixture was stirred for 1.5 h at 70 °C. All volatiles were removed under reduced pressure and the crude product was purified by recrystallization from a toluene solution. Yield: Quantitative. Electron ionization mass spectrometry (20 eV, 132 °C): *m/z* (intensity) 956 (10 %) 854 (74 %), 724 (17 %), 637 (12 %), 579 $[M]^+$ (100 %), 477 (15 %), 79 (89 %), 59 (48 %), 52 (20 %). Anal. Calcd $C_{34}H_{64}FeGdN_2O_6$: C 50.42, H 7.96, N 3.46. Found: C 47.03, H 8.09, N 2.44.

2.2. $GdFeO_3$ thin film growth

GFO films were prepared in a Cambridge Nanotech Savannah 100 flow-type ALD reactor. After optimization of the precursor sublimation temperature, the complex $[GdFe(O^tBu)_6(C_5H_5N)_2]$ was heated up to 150–170 °C for evaporation. Pulse/purge lengths for $[GdFe(O^tBu)_6(C_5H_5N)_2]$ and ozone were alternating pulsed into the reaction chamber as 0.2-1.0 s/1.5–3.0 s, respectively. A nitrogen gas flow of 40 sccm was used as carrier gas and for purging excess precursors and by-products. The substrate temperature was kept constant at 200 °C throughout the deposition process. 5 mm x 5 mm $SrTiO_3$ (STO) were used as a growth substrate and 1 cm x 1 cm Si(100) pieces were placed next to STO as reference substrates to perform SEM-EDX analysis. Before film growth, substrate surface was activated by 100 ozone pulses. Film thickness was tuned by modifying the number of cycles from 20 nm to 35 nm. The as-deposited films were further annealed for 30 min in oxygen atmosphere at 800 °C in a tubular furnace.

2.3. $GdFeO_3$ thin film characterization

Phase purity and film orientation were investigated from X-ray θ-2θ scans performed on a Bruker D8 Discover A25 diffractometer, with Cu Kα radiation. The film texture was further studied by a D8 Advance diffractometer with a General Area Detector Diffraction System with Cu Kα radiation, Bruker AXS, Inc. Energy Disperse X-ray Spectroscopy (EDX) and Scanning Electron Microscopy (SEM) FEI Quanta 200 FEG were used to study surface morphology and qualitative chemical composition. The operating voltage was 15 kV at 4×10^{-4} Pa. The acquisition time for the EDX analysis was set to 200 s. Surface chemical composition was explored by a SPECS PHOIBOS 150 hemispherical X-ray photoelectron spectroscopy (XPS) analyzer with an Al Kα source (1486.6 eV) from SPECS GmbH, Berlin, Germany. The measurements were performed in a base pressure of 1×10^{-8} Pa with a pass energy of 10 eV, and step size for the high-resolution and survey spectra were of 0.05 eV 30 and 1 eV, respectively. Spectra were calibrated referring to the binding energy of C1s peak at 284.8 eV. An Asylum Research MFP-3D Atomic Force Microscope (AFM) was employed for obtaining topographic images of $GdFeO_3$ film. Film thickness was determined by fitting the X-ray reflectivity data from a SIEMENS D5000 diffractometer using ReMagX software [40]. Magnetic properties of the films, M(T) and M(H), were explored using a Quantum Design MPMS-XL magnetometer based on a superconducting quantum interference device detector. Magnetic measurements were performed along the [001] film direction (in plane) and the diamagnetic contribution of the $SrTiO_3$ substrate was subtracted for all curves.

3. Results and discussion

3.1. Synthesis of heterobimetallic single-source precursor

The heteroleptic single source precursor $[GdFe(O^tBu)_6(C_5H_5N)_2]$ has been synthesized by using $[Fe(O^tBu)_3]_2$ and $[Gd\{N(SiMe_3)_2\}_3]$ in a molar ratio of 1:2. Both precursors have been dissolved in toluene and small amounts of pyridine. After mixing both solutions, *tert*-butanol has been added to result in the desired product. Iron and gadolinium ions prefer different coordination spheres when exposed to steric demanding ligands (Fe^{3+} = tetrahedral, Gd^{3+} = octahedral) due to different ionic radii (Fe^{3+} = 0.49 Å, Gd^{3+} = 0.94 Å) [41], therefore, special synthetic conditions are required to maintain both metal centers in a monomeric, heterobimetallic structure. In order to stabilize the octahedral coordination sphere of gadolinium and prevent oligomerization reactions, pyridine as a neutral ligand was added. Yellow/brownish single crystals were accessible and their analysis via X-ray diffractometry resulted in the presented molecular structure, see Fig. 1, Table 1. The polyhedron representation of the triclinic compound with a $P\bar{1}$ space group exhibits an edge sharing connected distorted octahedron around gadolinium and a distorted tetrahedron around iron. The nitrogen atoms are in a *trans* orientation and the bond length between gadolinium and nitrogen (Gd-N 2.551 Å) is longer than between gadolinium and oxygen (Gd-$O_{\mu 2}$ 2.428, Gd-$O_{terminal}$ 2.109), hinting to weakly bonded pyridine. The observed structure is very similar to literature known bimetallic iron/cerium compounds like $[FeCe(O^tBu)_7(C_5H_5N)]$ [42] and isotypic to $[FeEr(O^tBu)_6(C_5H_5N)_2]$ [43]. Both, cerium and erbium have similar large ionic radii compared to gadolinium (Ce^{4+} = 0.87 Å, Er^{3+} = 0.89 Å) [41]. The distance between gadolinium and the pyridine fragments is similar to the erbium compound and shorter than for

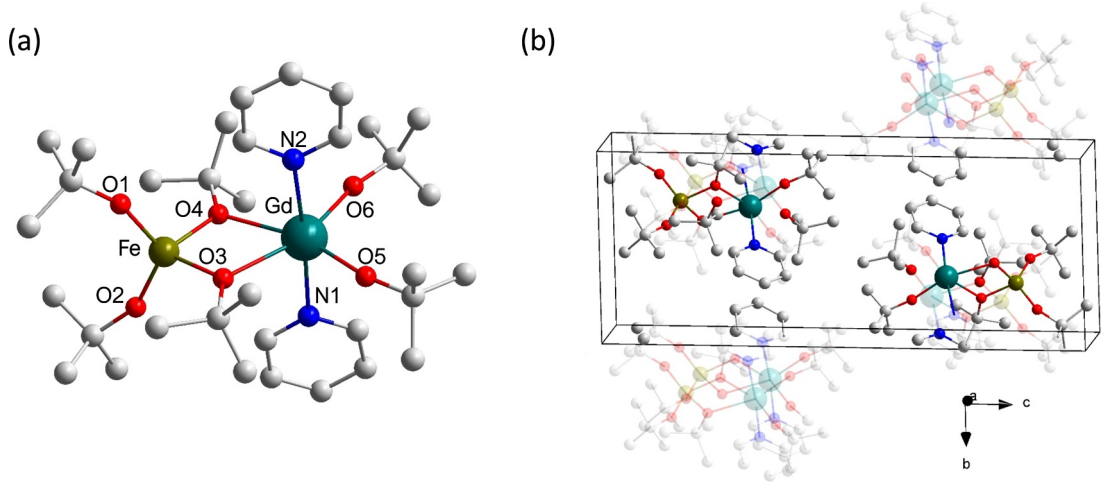

Fig. 1. (a) Molecular structure of $[GdFe(O^tBu)_6(C_5H_5N)_2]$, hydrogen atoms are omitted for clarity. Averaged selected bond lengths in [Å]: Gd – $O_{terminal}$ 2.109, Gd – $O_{\mu2}$ 2.428, Gd – N 2.551, Fe – $O_{terminal}$ 1.783, Fe – $O_{\mu2}$ 1.911. (b) Unit cell of the crystal structure. Two molecules are inside the unit cell, for a better understanding, every contributing molecule is shown but each atom not corresponding to the unit cell is transparent.

Table 1
Details on crystal and structure refinement of $[GdFe(O^tBu)_6(C_5H_5N)_2]$.

Molecular formula	$C_{34}H_{64}FeGdN_2O_6$
Molecular Mass [g/mol]	809.97
Temperature of Measurement [K]	170(2)
Wavelength [Å]	0.71073 (Mo K_α)
Crystal System	Triclinic
Space Group	P $\bar{1}$
Lattice Parameters	a = 9.4659(5) Å α = 86.285(4)° b = 10.2824(5) Å β = 82.418(4)° c = 23.0723(12) Å γ = 68.374(4)°
Cell Volume [$Å^3$]	2069.03(19)
Formula Unit	2
Correction of Absorption	numerical
F(000)	840
Measurement Range	1.781 < *h* < 26.804 −11 < h < 11 −13 < k < 13 −29 < l < 29
Number of Reflexes	23364
Observed Reflexes	8719
Goodness of Fit	1.103
R_1 [$I_o > 2\sigma(I)$]; all Data	R_1 = 0.0408, R_1 = 0.0560
wR_2 [$I_o > 2\sigma(I)$]; all Data	wR_2 = 0.0982, wR_2 = 0.1220
$\Delta\rho_{max}$, $\Delta\rho_{min}$	1.186, −1.771 e $Å^{-3}$

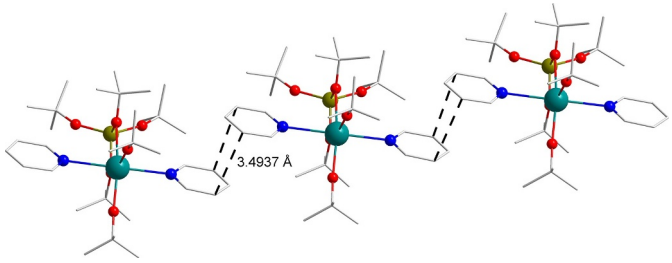

Fig. 2. Intermolecular, antiparallel π-stacking in the crystal structure of [GdFe $(OtBu)_6(C_5H_5N)_2$].

Table 2
Comparison of selected bond length and angles between $[GdFe(O^tBu)_6(C_5H_5N)_2]$ and literature known $[FeEr(O^tBu)_6(C_5H_5N)_2]$ and $[FeCe(O^tBu)_7(C_5H_5N)]$ [42,43].

	$[GdFe(O^tBu)_6(C_5H_5N)_2]$	$[FeEr(O^tBu)_6(C_5H_5N)_2]$	$[FeCe(O^tBu)_7(C_5H_5N)]$
Ln-$O_{term.}$	2.109 Å	2.047 Å	2.094 Å
Ln-$O_{\mu2}$	2.428 Å	2.366 Å	2.442 Å
Fe-$O_{term.}$	1.783 Å	1.771 Å	1.782 Å
Fe-$O_{\mu2}$	1.911 Å	1.914 Å	1.943 Å
Ln-N	2.551 Å	2.500 Å	2.700 Å
Ln-Fe	3.428 Å	3.401 Å	3.4739 Å
$O_{\mu2}$-Ln-$O_{\mu2}$	65.51°	65.94°	65.1°
$O_{\mu2}$-Fe-$O_{\mu2}$	86.87°	84.52°	85.7°
N-Gd-N	175.97°	174.08°	-

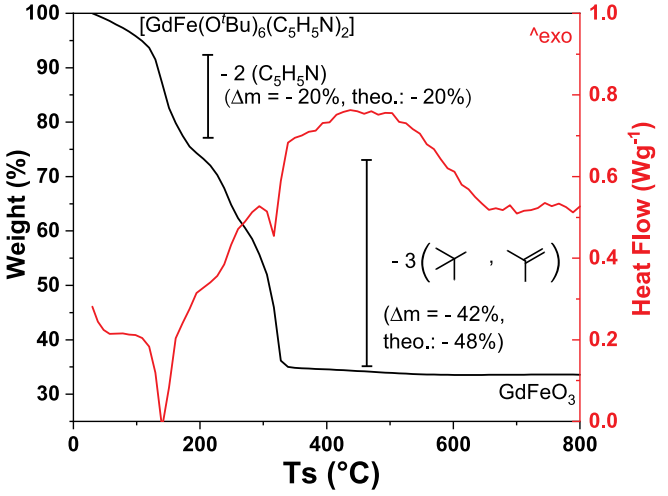

Fig. 3. Thermogravimetric analysis/ Differential scanning calorimetry diagram for $[GdFe(O^tBu)_6(C_5H_5N)_2]$. The compound undergoes a steady degradation towards $GdFeO_3$ (the remaining mass after measurement matches $GdFeO_3$). The missing 6 % mass loss of the second step can be attributed to the initial mass loss at low temperatures.

the cerium one, which can be attributed to the number of bound pyridine entities. In the crystal structure, the pyridine fragments arrange in an antiparallel π-stacking fashion with a distance between the aromatic rings of 3.494 Å (see Fig. 2). This feature is also known for the $[FeEr(O^tBu)_6(C_5H_5N)_2]$ complex [43]. A comparison between selected bond lengths and angles is given in Table 2.

The presented structure is in good agreement with the elemental analysis, thermogravimetry (Fig. 3) and mass spectrometry (Fig. 4). The compound exhibited a steady degradation process during heating with two clear endothermic transitions at 140 °C and 315 °C. Pyridine fragments evidently split from the molecule at the heating temperature

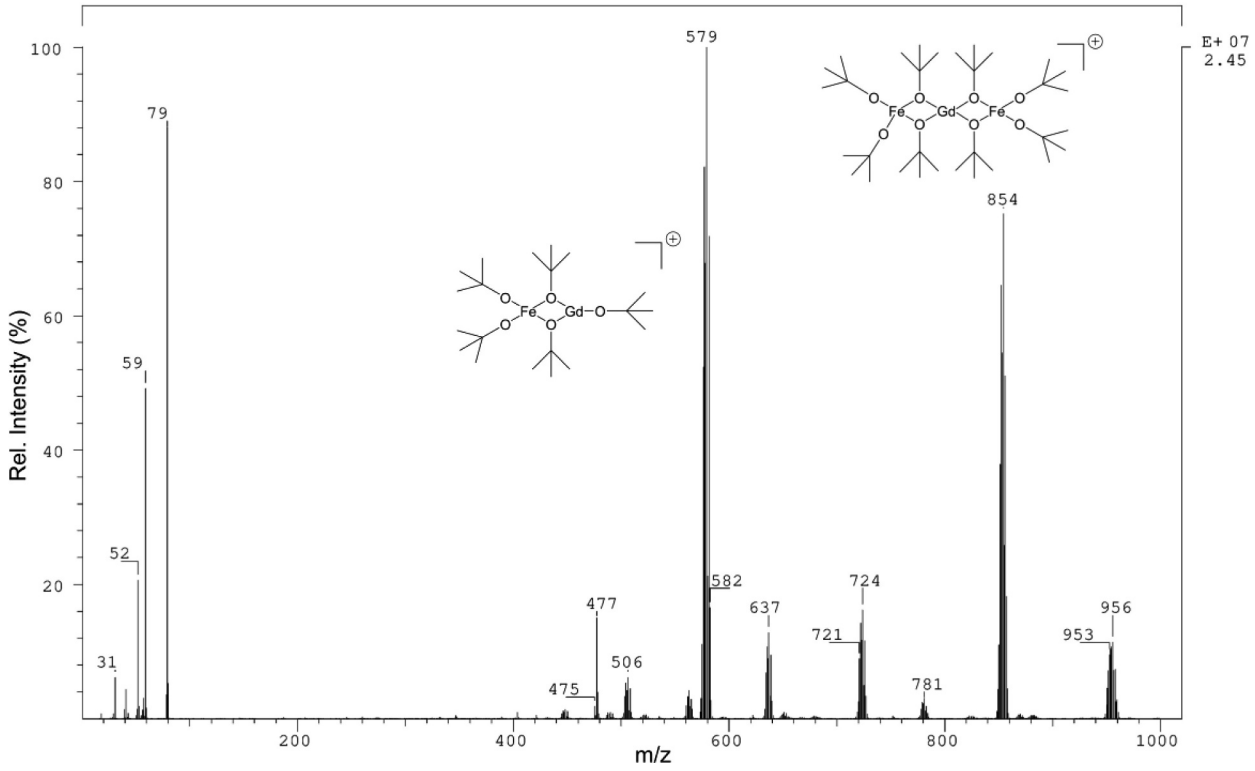

Fig. 4. Electron ionization mass spectra of $[GdFe(OtBu)_6(C_5H_5N)_2]$, ionized at U = 20 eV.

of 130 °C. The remaining mass at high temperatures was attributed to $GdFeO_3$ that based on the calculated weight loss (m: 33.4 %, theo.: 32.2 %) and no further events in the TG profile indicated the formation of solid of definite composition. The mass spectra (Electron ionization, 20 eV) confirmed the volatility and stability of the bimetallic component in the gas phase (Fig. 4). Even without showing the molecular ion peak $[M]^+$, the signal with the highest intensity corresponded to bimetallic fragment $[GdFe(O^tBu)_5]^+$ (579 m/z). The ionization energy during the measurement further induces oligomerization reactions apparently leading to fragments with higher molecular mass that were identified as $[Gd_2Fe_2O_2(O^tBu)_6(O^tBu\text{-}Me)]^+$ (956 m/z), $[GdFe_2(O^tBu)_8]^+$ (854 m/z), $[GdFe_2O(O^tBu)_6]^+$ (724 m/z) and $[Fe_2(O^tBu)_5]^+$ (477 m/z).

3.2. Thin film growth by ALD

GFO was deposited on $SrTiO_3$ (STO) at 200 °C by ALD and exposed to 800 °C to crystallize the orthoferrite structure with a film thickness of 20 nm. The film growth per deposition cycle was investigated at 200 °C showed a linear dependence with a growth rate of approximately 0.19 Å per cycle (see Fig. 5). The reported growth rates of ALD oxide thin films grown from single-source heterobimetallic precursors are broad. For instance, the ALD deposited rare earth aluminates prepared from Ln-Al (Ln = La, Pr, Nd) compounds showed growth per cycles (GPC) one order of magnitude higher (0.1-0.5 nm/cycle) than our current ALD $GdFeO_3$ study [44,45]. On the other hand, ALD $SrTa_2O_6$ thin film from a nitrogen-donor-functionalized Sr-Ta alkoxide exhibited GPC around 0.2–0.3 Å per cycle, similar to our work herein [46].

Fig. 6(a) compares the X-ray diffraction θ-2θ scans of bare strontium titanate substrates, STO (black), as-deposited GFO film (green) and post annealed GFO at 800 °C (blue). The as-deposited film showed no extra features except peaks corresponding to STO (001) and k_β, suggesting an amorphous deposited film. After post annealing, a shoulder emerged next to the STO peak at 2θ ~ 47°. A closer look at the GFO phase formation by performing a 2D θ-2θ scan (Fig. 6(b)), allowed the identification of two extra poles at 2θ = 26° (χ = +26° and χ = -27°). The

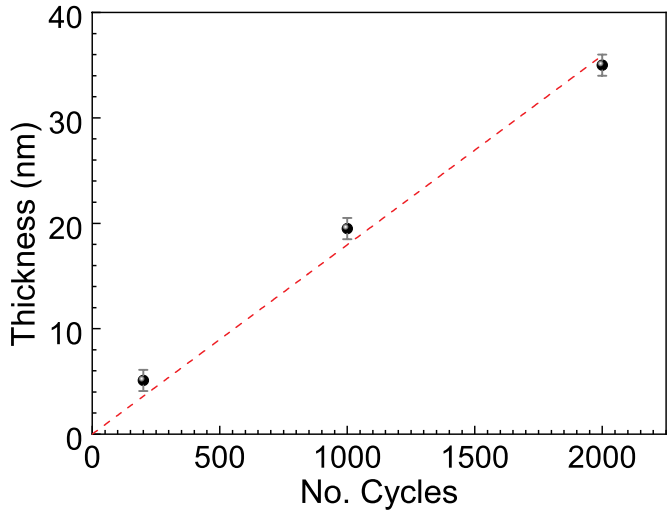

Fig. 5. Variation of $GdFeO_3$ film thickness with number of ALD cycles using Gd-Fe heterobimetallic precursor at a deposition temperature of 200 °C. The data was fitted linearly with the intercept forced to 0.

GFO has a slightly distorted ABO_3 perovskite structure with a = 5.346 Å, b = 5.616 Å, c = 7.668 Å whereas the dimensions of cubic $SrTiO_3$ are a = 3.905 Å. Based on this, it is very likely that orthorhombic GFO grows oriented (110)//[001] on STO. No traces of Fe_3O_4 and $Gd_3Fe_5O_{12}$ were observed [1,7,47].

Chemical composition of the as-deposited film was analyzed by EDX (Fig. 7) on GFO / Si (100) reference samples that confirmed the presence of Gd, Fe, Si and O with nearly an equivalent cation ratio (Fe: Gd = 0.9).

The chemical states of GFO thin films on STO was further analyzed by XPS (Fig. 8). The survey spectrum indicated the presence of Gd, Fe, O, C, Sr and Ti, consistent with the $GdFeO_3$ / $SrTiO_3$ structure (Fig. 8a). The presence of C is majorly attributed to the ambient exposure of the

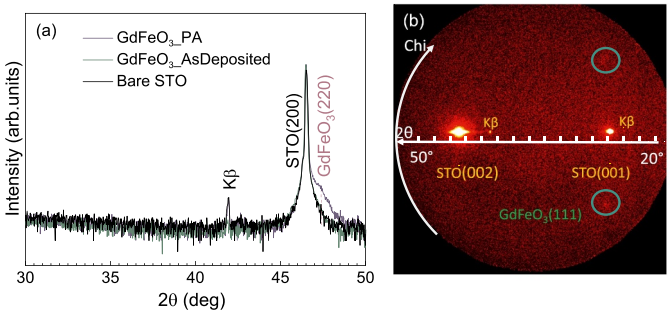

Fig. 6. (a) X-ray diffraction θ-2θ scan of ALD 20 nm thick $GdFeO_3$ films on $SrTiO_3$ (STO) after deposition and after post annealing (PA). (b) X-ray diffraction θ-2θ pattern of post-annealed 20 nm $GdFeO_3$ films on STO.

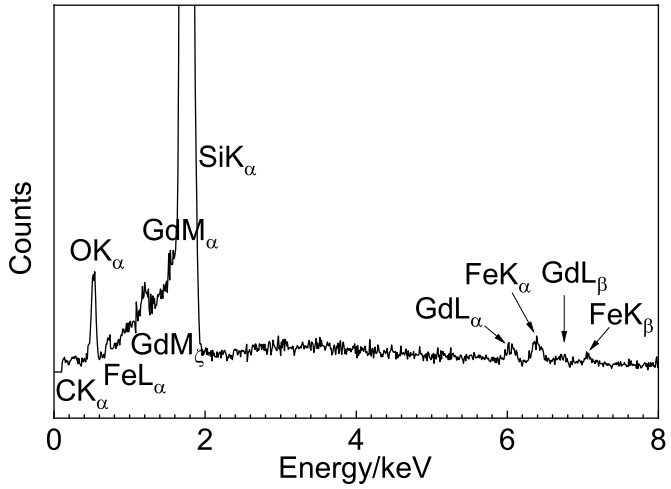

Fig. 7. EDX spectrum of ALD deposited $GdFeO_3$ thin films on (100) Si.

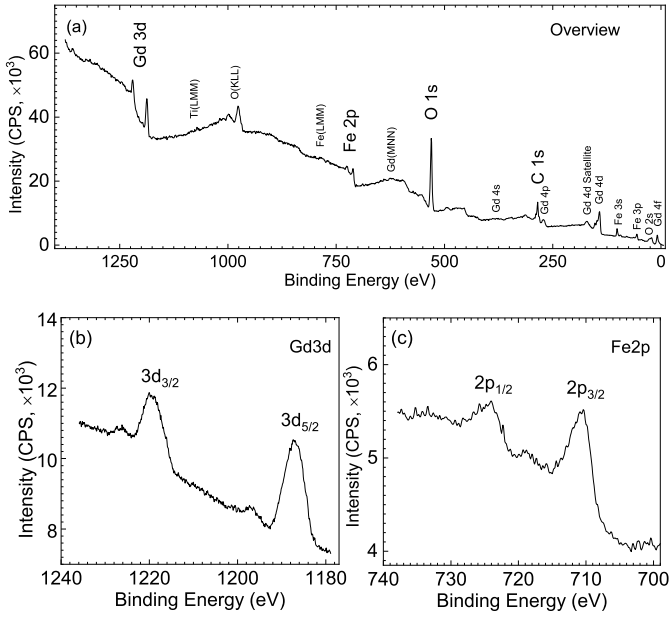

Fig. 8. XPS spectrum of ALD deposited 20 nm $GdFeO_3$ thin films on (100) STO: (a) Survey spectrum; (b) high resolution Gd(3d) core level spectrum (c) high resolution Fe(2p) core level spectrum.

samples prior to the XPS analysis. No traces of nitrogen were spotted in the film (binding energy N1s = 398.1 eV), suggesting a complete decomposition of the pyridine ligands present on the heterobimetallic

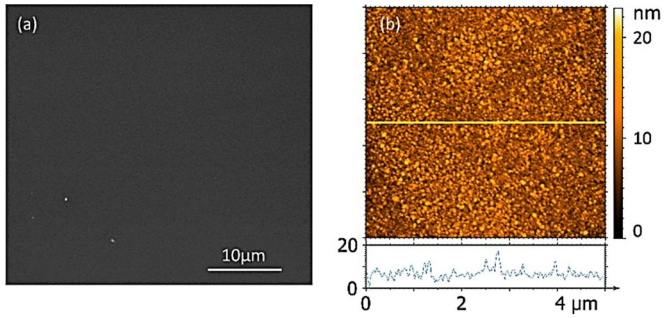

Fig. 9. (a) SEM image of ALD deposited 20 nm $GdFeO_3$ thin film on (100) Silicon; (b) AFM topographic image of post annealed 20 nm ALD $GdFeO_3$ thin film on (100) STO.

precursor. The Gd(3d) core level spectrum, Fig. 8(b), shows a spin-orbit doublet with binding energies at 1219.3 eV $3d_{3/2}$ and 1187.3 eV $3d_{5/2}$, being in good agreement with those reported in literature for $GdFeO_3$ and Gd_2O_3 [47,48]. Likewise, the Fe(2p) core level spectrum showed a peak at 724.1 eV $2p_{1/2}$ and at 710.6 eV $2p_{3/2}$. Moreover, the position of the satellite peak at 718.9 eV appearing 8.3 eV depicted in Fig. 8(c), above the $2p_{1/2}$ peak which confirms the +3 oxidation state of iron [47,49–51].

The morphology of ALD grown GFO has been studied by SEM and AFM. The sample is homogeneous in a large area as shown in the SEM image in Fig. 9(a). A 5 × 5 μm AFM topographic image and a height profile (indicated by the yellow line) are shown in Fig. 9(b). The topographic image revealed a homogeneous distribution of small grains (~70 nm) with a root mean square roughness of 2 nm.

The temperature dependent magnetization measurements (5-300 K) of GFO thin film on STO under zero field-cooling (ZFC) and field-cooling (FC) at 0.5 Tesla are shown in Fig. 10(a). In this case, thicker films (35 nm) were investigated. Both curves overlap and show no magnetic transition for this temperature range [47,52]. While the magnetization decreases with increasing temperature up to 300 K, the χ^{-1} (T) (χ being the magnetic susceptibility) shows initially an upward curvature and then at ~100 K changes to slightly negative curvature (inset Fig. 10(a)). This dependence in χ^{-1} suggests a ferromagnetic contribution overlapped with the paramagnetic behavior. Fig. 10(b) illustrates the field dependent magnetization curve at 50 K. The net saturation magnetization at 7 Tesla is 82.89 kA/m and the coercive field is 0.0078 Tesla. These values slightly differ from previous studies on GFO nanoparticles [7,53] but resemble those of sol-gel thin films [47] and single crystals [52], showing the difference in magnetic properties depending on the size and crystallinity [54]. Bulk gadolinium orthoferrite is known to be antiferromagnetic with a Néel temperature of 678 K [55]. The magnetic properties of GFO can be understood by the superposition of two independent magnetic systems, Gd^{3+} (paramagnetic contribution) and Fe^{3+} (ferromagnetic contribution) sublattices [55]. Thus, the weak ferromagnetism identified in this

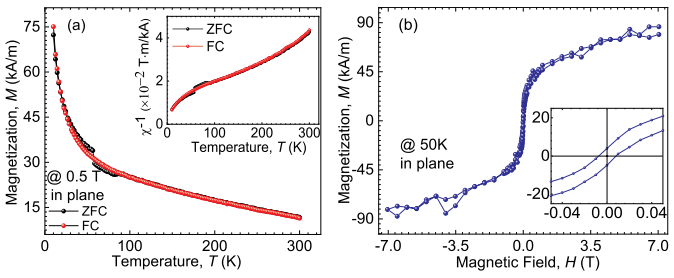

Fig. 10. (a) In-plane magnetization performance as a function of temperature for a 35 nm $GdFeO_3$ thin film. Inset shows the reverse susceptibility behavior versus temperature; (b) Magnetization behavior of 35 nm thick $GdFeO_3$ film as a function of magnetic field at 50 K. Inset shows a zoom-in at a lower field.

ALD fabricated $GdFeO_3$ system is tentatively attributed to slightly canted Fe^{3+} ions [52,56].

4. Conclusion

A volatile heteronuclear precursor $[GdFe(O^tBu)_6(C_5H_5N)_2]$ was demonstrated as an efficient single-source for the atomic layer deposition of ternary oxide $GdFeO_3$. The heterometallic framework is evidently maintained in the gas phase even after the thermolytic cleavage of the coordinated pyridine molecule that supports the formation of stoichiometric ternary oxide. The ALD with the mixed-metal compound on STO substrate with low lattice mismatch produced epitaxial films of $GdFeO_3$ that did not show the presence of impurities and minor phases like garnet ($Gd_3Fe_5O_{12}$), spinel ($GdFe_2O_4$) or magnetite (Fe_3O_4) compositions that are generally formed in the synthesis of $GdFeO_3$ performed using two monometallic precursors. Advances in precursor design for ALD and epitaxial growth opens a plethora of opportunities to engineer coatings with multimetallic compositions at low temperature and to understand the reaction kinetics which can ultimately improve the capabilities for thin films engineering.

CRediT authorship contribution statement

Christoph Bohr: Conceptualization, Methodology, Investigation, Writing - original draft. **Pengmei Yu:** Investigation, Writing - original draft. **Mateusz Scigaj:** Investigation. **Corinna Hegemann:** Conceptualization, Writing - review & editing. **Thomas Fischer:** Writing - review & editing. **Mariona Coll:** Methodology, Writing - review & editing, Supervision. **Sanjay Mathur:** Conceptualization, Writing - review & editing, Supervision.

Declaration of Competing Interest

The authors declare that they have no known competing financial interests or personal relationships that could have appeared to influence the work reported in this paper.

Acknowledgments

S.M. is thankful to the German Science Foundation (DFG) for the funding provided in the framework of the SPP Perovskites “SPP 2196/1 - Perovskite semiconductors: From fundamentalproperties to devices”. This work is supported by an Evonik foundation scholarship (C. Bohr). The authors gratefully acknowledge the financial supports through the “Severo Ochoa” Programme for Centres of Excellence in R&D (SEV-2015-0496), FUNMAT-FIP-2016- NANOSOLE project, and CHEMOX MAT2017-83169-R from the Spanish Ministry of Economy and Competitiveness. This article is based upon work from COST Action MP1402 “Hooking together European research in atomic layer deposition (HERALD)”, supported by COST (European Cooperation in Science and Technology).The authors want to thank Dr. Ingo Pantenburg for single crystal measurement, Astrid Baum for mass spectrometry measurements and the University of Cologne for financial and structural support, as well as the Scientific Services at ICMAB and G. Sauthier from ICN2 core support facilities for XPS analysis. This work is supported by the Chinese Scholarship Council (CSC fellowship 201606920073, P. Yu) and Ramón y Cajal program (RYC-2013-12448, M. Coll) .

References

[1] D.S. Schmool, N. Keller, M. Guyot, R. Krishnan, M. Tessier, Magnetic and magneto-optic properties of orthoferrite thin films grown by pulsed-laser deposition, J. Appl. Phys. 86 (1999) 5712–5717, https://doi.org/10.1063/1.371583.

[2] X. Niu, H. Li, G. Liu, Preparation, characterization and photocatalytic properties of $REFeO_3$ (RE = Sm, Eu, Gd), J. Mol. Catal. A Chem. 232 (2005) 89–93, https://doi.org/10.1016/j.molcata.2005.01.022.

[3] J. Tsagaroyannis, K.J. Haralambous, Z. Loizos, G. Petroutsos, N. Spyrellis, Gadolinium-iron ferrites: catalytic effect on the water-gas shift reaction, Mater. Lett. 28 (1996) 393–400, https://doi.org/10.1016/0167-577x(96)00089-4.

[4] J. Ding, X. Lü, H. Shu, J. Xie, H. Zhang, Microwave-assisted synthesis of perovskite $ReFeO_3$ (Re: La, Sm, Eu, Gd) photocatalyst, Mater. Sci. Eng. B Solid-State Mater. Adv. Technol. 171 (2010) 31–34, https://doi.org/10.1016/j.mseb.2010.03.050.

[5] M. Siemons, A. Leifert, U. Simon, Preparation and gas sensing characteristics of nanoparticulate p-Type semiconducting $LnFeO_3$ and $LnCrO_3$ materials, Adv. Funct. Mater. 17 (2007) 2189–2197, https://doi.org/10.1002/adfm.200600454.

[6] X. Niu, W. Du, W. Du, Preparation, characterization and gas-sensing properties of rare earth mixed oxides, Sens. Actuat. B Chem. 99 (2004) 399–404, https://doi.org/10.1016/j.snb.2003.12.006.

[7] F. Söderlind, M.A. Fortin, R.M. Petoral Jr, A. Klasson, T. Veres, M. Engström, K. Uvdal, P.-O. Käll, Colloidal synthesis and characterization of ultrasmall perovskite $GdFeO_3$ nanocrystals, Nanotechnology 19 (2008) 085608, , https://doi.org/10.1088/0957-4484/19/8/085608.

[8] N. Kimizuka, A. Yamamoto, H. Ohashi, T. Sugihara, T. Sekine, The stability of the phases in the Ln_2O_3-FeO-Fe_2O_3 systems which are stable at elevated temperatures (Ln: Lanthanide Elements and Y), J. Solid State Chem. 49 (1983) 65–76, https://doi.org/10.1016/0022-4596(83)90217-7.

[9] S. Geller, Crystal structure of gadolinium orthoferrite, $GdFeO_3$, J. Chem. Phys. 24 (1956) 1236–1239, https://doi.org/10.1063/1.1742746.

[10] I. Warshaw, R. Roy, Stable and metastable equilibria in the systems Y_2O_3-Al_2O_3, and Gd_2O_3-Fe_2O_3, J. Am. Ceram. Soc. 42 (1959) 434–438, https://doi.org/10.1111/j.1151-2916.1959.tb12970.x.

[11] H.J. Van Hook, Phase relations in the system Fe_2O_3–Fe_3O_4–$YFeO_3$ in air, J. Am. Ceram. Soc. 44 (1961) 208–214, https://doi.org/10.1111/j.1151-2916.1961.tb15362.x.

[12] R.W. Johnson, A. Hultqvist, S.F. Bent, A brief review of atomic layer deposition: from fundamentals to applications, Mater. Today 17 (2014) 236–246, https://doi.org/10.1016/j.mattod.2014.04.026.

[13] I. Azpitarte, A. Zuzuarregui, H. Ablat, L. Ruiz-Rubio, A. López-Ortega, S.D. Elliott, M. Knez, Suppressing the thermal and ultraviolet sensitivity of kevlar by infiltration and hybridization with ZnO, Chem. Mater. 29 (2017) 10068–10074, https://doi.org/10.1021/acs.chemmater.7b03747.

[14] N.T. Eigenfeld, J.M. Gray, J.J. Brown, G.D. Skidmore, S.M. George, V.M. Bright, Ultra-thin 3D nano-devices from atomic layer deposition on polyimide, Adv. Mater. 26 (2014) 3962–3967, https://doi.org/10.1002/adma.201400410.

[15] J. Bachmann, Atomic Layer Deposition in Energy Conversion Applications, first ed., Wiley-VCH, 2017.

[16] K.B. Klepper, O. Nilsen, H. Fjellvåg, Growth of thin films of Co_3O_4 by atomic layer deposition, Thin Solid Films 515 (2007) 7772–7781, https://doi.org/10.1016/j.tsf.2007.03.182.

[17] O. Nilsen, E. Rauwel, H. Fjellvåg, A. Kjekshus, Growth of $La_{1-x}Ca_xMnO_3$ thin films by atomic layer deposition, J. Mater. Chem. 17 (2007) 1466–1475, https://doi.org/10.1039/B616982A.

[18] M. Coll, J. Gazquez, A. Palau, M. Varela, X. Obradors, T. Puig, Low temperature epitaxial oxide ultrathin films and nanostructures by atomic layer deposition, Chem. Mater. 24 (2012) 3732–3737, https://doi.org/10.1021/cm301864c.

[19] J.A. Klug, N.G. Becker, N.R. Groll, C. Cao, M.S. Weimer, M.J. Pellin, J.F. Zasadzinski, T. Proslier, Heteroepitaxy of group IV-VI nitrides by atomic layer deposition, Appl. Phys. Lett. 103 (2013) 1–5, https://doi.org/10.1063/1.4831977.

[20] V. Miikkulainen, M. Leskelä, M. Ritala, R.L. Puurunen, Crystallinity of inorganic films grown by atomic layer deposition: overview and general trends, J. Appl. Phys. 113 (2013) 021301, , https://doi.org/10.1063/1.4757907.

[21] M. Coll, J.M. Montero Moreno, J. Gazquez, K. Nielsch, X. Obradors, T. Puig, Low temperature stabilization of nanoscale epitaxial spinel ferrite thin films by atomic layer deposition, Adv. Funct. Mater. 24 (2014) 5368–5374, https://doi.org/10.1002/adfm.201400517.

[22] M. Coll, J. Gazquez, I. Fina, Z. Khayat, A. Quindeau, M. Alexe, M. Varela, S. Trolier-McKinstry, X. Obradors, T. Puig, Nanocrystalline ferroelectric $BiFeO_3$ thin films by low-temperature atomic layer deposition, Chem. Mater. 27 (2015) 6322–6328, https://doi.org/10.1021/acs.chemmater.5b02093.

[23] H.H. Sønsteby, H. Fjellvåg, O. Nilsen, Functional perovskites by atomic layer deposition - an overview, Adv. Mater. Interfaces. 4 (2017) 1600903.

[24] A. Devi, Old Chemistries‘ for new applications: perspectives for development of precursors for MOCVD and ALD applications, Coord. Chem. Rev. 257 (2013) 3332–3384, https://doi.org/10.1016/j.ccr.2013.07.025.

[25] S.T. Barry, Amidinates, guanidinates and iminopyrrolidinates: understanding precursor thermolysis to design a better ligand, Coord. Chem. Rev. 257 (2013) 3192–3201, https://doi.org/10.1016/j.ccr.2013.03.015.

[26] M. Leskelä, M. Ritala, O. Nilsen, Novel materials by atomic layer deposition and molecular layer deposition, MRS Bull. 36 (2011) 877–884.

[27] P. De Rouffignac, R.G. Gordon, Atomic layer deposition of praseodymium aluminum oxide for electrical applications, Chem. Vap. Depos. 12 (2006) 152–157, https://doi.org/10.1002/cvde.200506377.

[28] M. Coll, M. Napari, Atomic layer deposition of multicomponent functional oxides, APL Mater. 7 (2019) 110901, , https://doi.org/10.1063/1.5113656.

[29] P. Marchand, C.J. Carmalt, Molecular precursor approach to metal oxide and pnictide thin films, Coord. Chem. Rev. 257 (2013) 3202–3221, https://doi.org/10.1016/j.ccr.2013.01.030.

[30] K. Bernal Ramos, M.J. Saly, Y.J. Chabal, Precursor design and reaction mechanisms for the atomic layer deposition of metal films, Coord. Chem. Rev. 257 (2013) 3271–3281, https://doi.org/10.1016/j.ccr.2013.03.028.

[31] T. Hatanpää, M. Ritala, M. Leskelä, Precursors as enablers of ALD technology: contributions from University of Helsinki, Coord. Chem. Rev. 257 (2013)

3297–3322, https://doi.org/10.1016/j.ccr.2013.07.002.
[32] S. Mathur, M. Veith, H. Shen, S. Hu, Structural and optical properties of $NdAlO_3$ nanocrystals embedded in an Al_2O_3 matrix, Chem. Mater. 14 (2002) 568–582.
[33] D.B.G. Williams, M. Lawton, Drying of organic solvents: quantitative evaluation of the efficiency of several desiccants, J. Org. Chem. 75 (2010) 8351–8354, https://doi.org/10.1021/jo101589h.
[34] S. Mathur, M. Veith, V. Sivakov, H. Shen, H.B. Gao, Composition, morphology and particle size control in nanocrystalline iron oxide films grown by single-source CVD, J. Phys. IV. 11 (2001) 487–494, https://doi.org/10.1051/jp4:2001362.
[35] D.C. Bradley, J.S. Ghotra, F.A. Hart, Three-co-ordination in lanthanide chemistry: Tris[bis(trimethylsilyl)amido]lanthanide(III) compounds, J. Chem. Soc. Chem. Commun. (1972) 349–350.
[36] Stoe & Cie GmbH Darmstadt Deutschland, X-RED32 1.31 (2005) & X-SHAPE 1.06; 1999., X-RED32 1.31 X-SHAPE 1.06, (1999).
[37] L.J. Farrugia, *WinGX* suite for small-molecule single-crystal crystallography, J. Appl. Crystallogr. 32 (1999) 837–838, https://doi.org/10.1107/S0021889899006020.
[38] A. Altomare, G. Cascarano, C. Giacovazzo, A. Guagliardi, M.C. Burla, G. Polidori, M. Camalli, SIRPOW .92 – a program for automatic solution of crystal structures by direct methods optimized for powder data, J. Appl. Crystallogr. 27 (1994) 435–436, https://doi.org/10.1107/S0021889894000221.
[39] G.M. Sheldrick, A short history of SHELX, Acta Crystallogr. Sect. A Found. Crystallogr. 64 (2007) 112–122, https://doi.org/10.1107/S0108767307043930.
[40] S. Macke, A. Radi, J.E. Hamann-Borrero, A. Verna, M. Bluschke, S. Brück, E. Goering, R. Sutarto, F. He, G. Cristiani, M. Wu, E. Benckiser, H.U. Habermeier, G. Logvenov, N. Gauquelin, G.A. Botton, A.P. Kajdos, S. Stemmer, G.A. Sawatzky, M.W. Haverkort, B. Keimer, V. Hinkov, Element specific monolayer depth profiling, Adv. Mater. 26 (2014) 6554–6559, https://doi.org/10.1002/adma.201402028.
[41] R.D. Shannon, Revised effective ionic radii and systematic studies of interatomic distances in halides and chalcogenides, Acta Crystallogr. Sect. A 32 (1976) 751–767, https://doi.org/10.1107/S0567739476001551.
[42] J. Schläfer, S. Stucky, W. Tyrra, S. Mathur, heterobi- and trimetallic cerium(iv) tert-butoxides with mono-, di-, and trivalent metals (M = K(I), Ge(II), Sn(II), Pb(II), Al (III), Fe(III)), Inorg. Chem. 52 (2013) 4002–4010, https://doi.org/10.1021/ic400030j.
[43] J. Schläfer, Neuartige Homo- und Heterometallische Cer-Alkoxide (in German), PhD Thesis University of Cologne, 2014.
[44] J.M. Gaskell, A.C. Jones, H.C. Aspinall, S. Przybylak, P.R. Chalker, K. Black, H.O. Davies, P. Taechakumput, S. Taylor, G.W. Critchlow, Liquid injection ALD and MOCVD of lanthanum aluminate using a bimetallic alkoxide precursor, J. Mater. Chem. 16 (2006) 3854–3860, https://doi.org/10.1039/b609129f.
[45] J.M. Gaskell, S. Przybylak, A.C. Jones, H.C. Aspinall, P.R. Chalker, K. Black, R.J. Potter, P. Taechakumput, S. Taylor, Deposition of Pr- and Nd-aluminate by liquid injection MOCVD and ALD using single-source heterometallic alkoxide precursors, Chem. Mater. 19 (2007) 4796–4803, https://doi.org/10.1021/cm0707556.
[46] M. Vehkamäki, M. Ritala, M. Leskelä, A.C. Jones, H.O. Davies, T. Sajavaara, E. Rauhala, Atomic layer deposition of strontium tantalate thin films from bimetallic precursors and water, J. Electrochem. Soc. 151 (2004) F69–F72, https://doi.org/10.1149/1.1648025.
[47] F. Söderlind, L. Selegård, P. Nordblad, K. Uvdal, P.O. Käll, Sol-gel synthesis and characterization of polycrystalline $GdFeO_3$ and $Gd_3Fe_5O_{12}$ thin films, J. Sol-Gel Sci. Technol. 49 (2009) 253–259, https://doi.org/10.1007/s10971-008-1859-0.
[48] D. Raiser, J.P. Deville, Study of XPS photoemission of some gadolinium compounds, J. Electron Spectros. Relat. Phenomena. 57 (1991) 91–97, https://doi.org/10.1016/0368-2048(91)85016-M.
[49] A.P. Grosvenor, B.A. Kobe, M.C. Biesinger, N.S. McIntyre, Investigation of multiplet splitting of Fe 2p XPS spectra and bonding in iron compounds, Surf. Interface Anal. 36 (2004) 1564–1574, https://doi.org/10.1002/sia.1984.
[50] E. Paparazzo, Xps analysis of iron aluminum oxide systems, Appl. Surf. Sci. 25 (1986) 1–12.
[51] P.C.J. Graat, M.A.J. Somers, Simultaneous determination of composition and thickness of thin iron-oxide films from XPS Fe 2p spectra, Appl. Surf. Sci. 100–101 (1996) 36–40, https://doi.org/10.1016/0169-4332(96)00252-8.
[52] P. Ramesh Babu, I. Bhaumik, S. Ganesamoorthy, S. Kalainathan, R. Bhatt, A.K. Karnal, P.K. Gupta, Investigation of magnetic property of $GdFeO_3$ single crystal grown in air by optical floating zone technique, J. Alloys Compd. 631 (2015) 232–236, https://doi.org/10.1016/j.jallcom.2015.01.112.
[53] S. Mathur, H. Shen, N. Lecerf, A. Kjekshus, H. Fjellvåg, G.F. Goya, Nanocrystalline orthoferrite $GdFeO_3$ from a novel heterobimetallic precursor, Adv. Mater. 14 (2002) 1405–1409.
[54] S. Carmen-Gabriela, From Bulk to Nano: The Many Sides of Magnetism, 1st ed., Springer, 2008, https://doi.org/10.1007/978-3-540-70548-2.
[55] M.a. Gilleo, Magnetic properties of a gadolinium orthoferrite, $GdFeO_3$, crystal, J. Chem. Phys. 24 (1956) 1239–1243, https://doi.org/10.1063/1.1742747.
[56] R.M. Bozorth, Origin of weak ferromagnetism in rare-earth orthoferrites, Phys. Rev. Lett. 1 (1958) 362–363, https://doi.org/10.1103/PhysRevLett.1.362.